Title
Geodetic Observations of Weak Determinism in Rupture Evolution of Large Earthquakes.

Journal
Journal of geophysical research. Solid earth, 123(11)

ISSN
2169-9313

Authors
Goldberg, DE
Melgar, D
Bock, Y
et al.

Publication Date
2018-11-01

DOI
10.1029/2018jb015962

Peer reviewed

Journal of Geophysical Research: Solid Earth

RESEARCH ARTICLE
10.1029/2018JB015962

Key Points:
- GNSS observations in addition to seismic observations are critical to rapid and reliable earthquake magnitude estimates
- GNSS-derived displacements can reliably estimate earthquake magnitude prior to rupture completion
- Evidence of weak determinism suggests that near-fault instrumentation is the best method for improving rapid magnitude estimations

Supporting Information:
- Supporting Information S1

Correspondence to:
D. E. Goldberg,
degoldberg@ucsd.edu

Citation:
Goldberg, D. E., Melgar, D., Bock, Y., & Allen, R. M. (2018). Geodetic observations of weak determinism in rupture evolution of large earthquakes. *Journal of Geophysical Research: Solid Earth*, *123*, 9950–9962. https://doi.org/10.1029/2018JB015962

Received 13 APR 2018
Accepted 31 OCT 2018
Accepted article online 5 NOV 2018
Published online 27 NOV 2018

Geodetic Observations of Weak Determinism in Rupture Evolution of Large Earthquakes

D. E. Goldberg[1], D. Melgar[2], Y. Bock[1], and R. M. Allen[3]

[1]Institute of Geophysics and Planetary Physics, Scripps Institution of Oceanography, University of California, San Diego, CA, USA, [2]Department of Earth Sciences, University of Oregon, Eugene, OR, USA, [3]Berkeley Seismological Laboratory, University of California, Berkeley, CA, USA

Abstract The moment evolution of large earthquakes is a subject of fundamental interest to both basic and applied seismology. Specifically, an open problem is when in the rupture process a large earthquake exhibits features dissimilar from those of a lesser magnitude event. The answer to this question is of importance for rapid, reliable estimation of earthquake magnitude, a major priority of earthquake and tsunami early warning systems. Much effort has been made to test whether earthquakes are deterministic, meaning that observations in the first few seconds of rupture can be used to predict the final rupture extent. However, results have been inconclusive, especially for large earthquakes greater than M_w7. Traditional seismic methods struggle to rapidly distinguish the size of large-magnitude events, in particular near the source, even after rupture completion, making them insufficient to resolve the question of predictive rupture behavior. Displacements derived from Global Navigation Satellite System data can accurately estimate magnitude in real time, even for the largest earthquakes. We employ a combination of seismic and geodetic (Global Navigation Satellite System) data to investigate early rupture metrics, to determine whether observational data support deterministic rupture behavior. We find that while the earliest metrics (~5 s of data) are not enough to infer final earthquake magnitude, accurate estimates are possible within the first tens of seconds, prior to rupture completion, suggesting a weak determinism. We discuss the implications for earthquake source physics and rupture evolution and address recommendations for earthquake and tsunami early warning.

1. Introduction

The temporal evolution of seismic moment release is a subject of fundamental interest in earthquake source physics and applied seismology, particularly for large and damaging events. Specifically, whether a large earthquake presents characteristics different from an earthquake of lesser magnitude at some point during the seismic rupture has been widely debated. Observations have suggested that there is strong determinism; that is, it should be possible to estimate the final magnitude of an event in the first few seconds (the nucleation phase) of large rupture (e.g., Colombelli et al., 2014; Olson & Allen, 2005; Zollo et al., 2006). However, this hypothesis has been disputed. An observational basis has also been found for the contrasting view that there is no determinism whatsoever and that nucleation is a magnitude-independent process (e.g., Rydelek & Horiuchi, 2006) such that the final magnitude cannot be determined from observations of only the first few seconds of rupture. In particular, Meier et al. (2016) make a strong case for this universal, magnitude-independent nucleation by analyzing near-field strong-motion records for moderate events ($4.0 < M_w < 8.5$), finding no evidence that rupture onsets can be used to predict final magnitude. Recently, analyses of large databases of finite fault models obtained from teleseismic inversions have also been studied to shed light on these issues and have led to a more nuanced perspective. Melgar and Hayes (2017) find evidence that large events behave as self-similar slip pulses (Heaton, 1990) and propose a model of *weak determinism* for rupture evolution. In this view, sometime following nucleation (tens of seconds) rupture organizes into a self-similar pulse whose properties are diagnostic of final magnitude. Meier et al. (2017), analyzing the same data set, suggest a similar model but argue that rupture can only be distinguished once peak moment rate occurs, roughly a third of the way into a large rupture. Underlying these recent studies is a shift in the hypothesis being tested away from whether rupture nucleation is deterministic and toward when, following nucleation, information of the rupture evolution can be used to infer final magnitude.

These theoretical and observational considerations, which have made the problem difficult to solve, are further compounded by measurement challenges. Observing large earthquakes at close distances is not without difficulties. Inertial seismometers with both low and high gains are the most commonly used tool for regional earthquake observations. High-gain, broadband instruments are more sensitive to small ground motions, but their dynamic range is exceeded during heavy shaking, rendering their recordings unusable in the near field of large-magnitude events. Low-gain accelerometers capture the strongest shaking but are unable to distinguish between rotational and translational motions. As earthquakes get larger in magnitude, rotational motions become more important (Trifunac & Todorovska, 2001), leading to an inaccurate representation of ground motion, particularly at long periods. These errors in measurement, referred to as baseline offsets, are corrected in real time with high-pass filtering (e.g., Boore et al., 2002). This correction dampens the influence of the baseline offsets but leads to a band-limited signal that excludes the permanent displacement (the 0-Hz static offset), as well as the long-period band of the record. Furthermore, it reduces the observed amplitude of maximum displacement (e.g., Melgar et al., 2015). The consequence is that with traditional seismic observations, the magnitude of large, destructive earthquakes is often underestimated—even after rupture is complete—in a well-documented condition known as magnitude saturation (e.g., Colombelli et al., 2012; Hoshiba & Ozaki, 2014).

Saturation is of practical importance because rapid magnitude calculation has implications for seismic hazard mitigation. Once evaluated, magnitude, coupled with a suitable ground motion prediction equation, is the main measure used by early warning systems to provide an estimate of expected shaking at a given location before it occurs (e.g., Kohler et al., 2017). Prompt and accurate assessments of an earthquake's size and expected ground motion are also useful for first responders as an initial estimate of the extent of damage. At subduction zone regions, current local tsunami warning systems are driven simply by location and magnitude (Hoshiba & Ozaki, 2014). Magnitude uncertainties can inhibit the effectiveness of an early warning and particularly a tsunami evacuation order, because the predicted damage and affected areas will be underestimated. A poignant example was observed during the 2011 M_w9.1 Tohoku-oki earthquake offshore Japan (Yun & Hamada, 2014). The earthquake was estimated as M_w8.1, 122 s after origin and upgraded to M_w8.4 only after 74 min, at which point the tsunami had already inundated parts of the coast nearest to the source. When the earthquake was finally observed at teleseismic distances, the magnitude was upgraded to M_w9.1 (Hoshiba & Ozaki, 2014).

In an effort to overcome magnitude saturation and improve warnings, a considerable amount of attention has been devoted to other ground motion measurements. In particular, Global Navigation Satellite System (GNSS) observations can provide high-rate broadband displacements (Bock et al., 2011) devoid of baseline offsets and reliable down to the longest periods (Melgar et al., 2012). However, high-rate GNSS data have a lower sensitivity than seismic instrumentation: ~1–2 cm in the horizontal and ~5–10 cm in the vertical (Genrich & Bock, 2006). Therefore, GNSS data are not suitable for detection of the small-amplitude *P* wave arrivals, inhibiting the ability of utilizing such data to effectively pinpoint the timing of early rupture evolution. Furthermore, GNSS data are typically sampled at much lower sampling rates (1–10 Hz), primarily due to the verbosity of phase and pseudorange observations to multiple satellites at multiple wavelengths for each epoch. Seismogeodesy, the optimal combination of collocated seismic and geodetic instrumentation, provides a favorable data set for exploring the subtleties of early observations (Bock et al., 2011; Crowell et al., 2013; Goldberg & Bock, 2017; Melgar et al., 2012; Saunders et al., 2016). The combination data set has the temporal resolution of the seismic instrumentation and results in a displacement time series that is more accurate than that using integrated and filtered seismic instrumentation, and with reduced noise compared to GNSS-only, improving the sensitivity. Importantly, this approach enables the detection of *P* wave arrivals in seismogeodetic velocities, improving the timeliness of a warning (Goldberg & Bock, 2017). Algorithms that leverage these broadband displacement data and use them for magnitude calculation have been developed as well. Crowell et al. (2013) first noted that peak ground displacement (PGD) measured with seismogeodetic instrumentation is reliable for a simple point-source magnitude scaling law and Melgar et al. (2015) confirmed for a global suite of large events measured with geodetic instrumentation, that no saturation is observed in PGD with respect to either magnitude or source-to-station distance. Based on these observations, Crowell et al. (2016) designed and implemented a real-time PGD magnitude algorithm for the west coast of the United States. By their very nature, magnitude algorithms that rely on PGD scaling laws are limited in solution speed, because the peak displacement occurs

sometime after *S* waves arrive at a station, often many tens of seconds behind the *P* wave. However, Melgar et al. (2015) noted that, in particular, when stations are close to the source such as in the 2010 M_w8.8 Maule earthquake, PGD algorithms produced reliable magnitude estimates in ~60 s—well before the source process is complete (~150 s). Melgar and Hayes (2017) later reasoned that this was consistent with the weakly deterministic self-similar slip pulse model of rupture and that PGD should occur at near-source sites as soon as the slip pulse has propagated close to it and before the source process is complete. The magnitude-dependent temporal evolution of displacement ground motion amplitude has previously been investigated using strong-motion seismic instrumentation (e.g., Colombelli et al., 2014). However, an assessment of the time behavior of geodetically-derived PGD has not been carried out. High-rate GNSS and seismogeodetic networks are still evolving, and thus, there are only limited data sets. The only other synthesis of PGD observations (Melgar et al., 2015) includes 10 earthquakes across multiple tectonic settings, with only a few recordings for some events.

In this work, we present a systematic assessment of the temporal evolution of geodetically-derived PGD, which we refer to as PGD(*t*) and discuss its implications for the weak determinism model of rupture evolution and for rapid magnitude calculation and early warning. We limit the geographic reach of our study to Japan, reducing major global variation, and utilize the very dense GNSS Earth Observation Network operated by the Geospatial Information Authority (www.gsi.go.jp). We present the results from 14 medium- to large-magnitude events, M_w5.7–9.1 (Figure 1), each observed by between 177 and 700 GNSS stations (Table 1). Note that for this study we have only used Global Positioning System (GPS) observations but will continue to use the term *GNSS*, as observations from any other satellite constellation could be implemented in the same fashion. To maximize the number of observations, we produce 1-Hz GNSS waveforms for each event and time-align them to *P* wave arrival times by interpolating arrivals from the overlapping strong-motion networks (KiK-net and K-net) operated by the National Research Institute for Earth Science and Disaster Resilience (www.kyoshin.bosai.go.jp). From these dense displacement observations, we show that PGD(*t*) is consistent with the weak determinism model. While initially PGD(*t*) behaves the same for events of all magnitudes, in the first tens of seconds, before the source is complete, there is clear separation in PGD(*t*) as a function of final magnitude. Finally, we create synthetic kinematic rupture models for thrust faults to demonstrate the rupture characteristics that contribute to early identification of magnitude and provide recommendations for bolstering early warning efforts in light of our findings.

2. Data Sets

In order to study the temporal evolution of PGD we acquired 1-Hz RINEX data from Geospatial Information Authority GNSS stations in Japan for 14 earthquakes. The data acquired were for ~1,200 GNSS Earth Observation Network stations, shown in Figure 1 (purple triangles) along with the locations of the 14 earthquakes included in the study. Earthquake details are given in Table 1. The earthquakes occurred between 2003 and 2016, with magnitudes between M_w5.7 and M_w9.1. We processed the GNSS data using precise point positioning (Geng et al., 2013; Zumberge et al., 1997). Because the onset *P* wave amplitudes are usually below GNSS noise, we needed an alternative way of determining the start of the GNSS displacement record at each site. To that end, we relied on the very dense K-NET and KiK-net strong-motion networks. For each event, the *P* wave arrival times were manually picked from the vertical waveforms of all available strong-motion sites. The Japanese strong-motion networks are operated in triggered mode, and unfortunately, in some cases records begin after the *P* wave arrivals. Incomplete records like these were excluded. We use the *P* wave arrival times at seismic sites to time-align the GNSS waveforms. In this analysis of PGD evolution, we considered all GNSS stations contained within the geographic footprint described by the properly triggered strong-motion sites, relaxing the constraint that GNSS stations be collocated with a strong-motion accelerometer. There are many GNSS stations with clear displacement waveforms, but without nearby strong-motion station coverage from which we could sufficiently determine the *P* wave onsets at that GNSS location. These sites were not considered in our analysis (e.g., Figure 2). This reduces the number of available sites from ~1,200 in the entire GNSS network to anywhere between 177 and 700 for each event (Table 1 and Figures 2 and S1–S13 in the supporting information). The hypocentral distance, *R*, of each source station pair was computed from the catalog hypocenter location determined by the National Research Institute for Earth Science and Disaster Resilience.

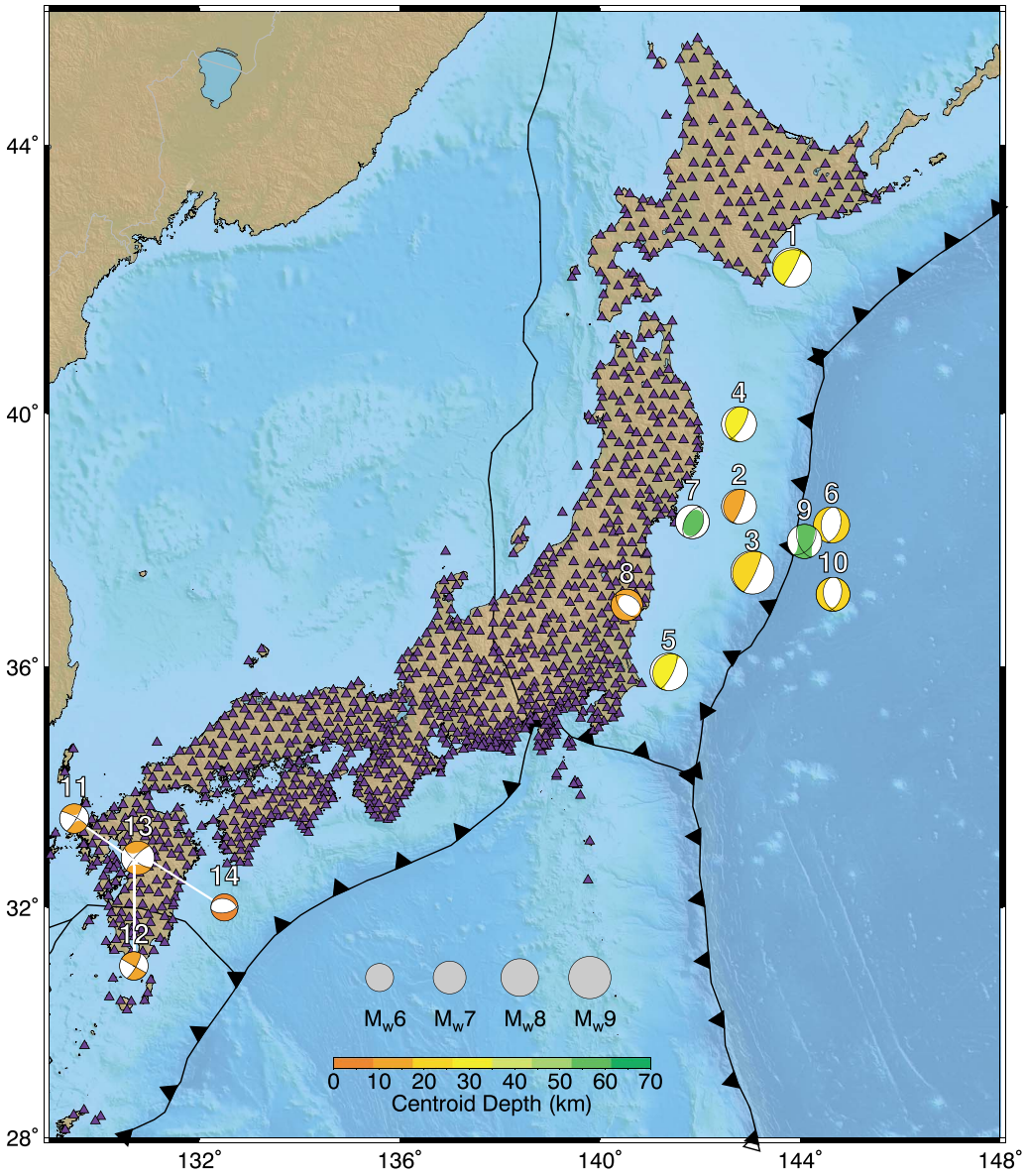

Figure 1. Map showing the locations of Global Navigation Satellite System Earth Observation Network stations (purple triangles) and the 14 earthquakes (focal mechanisms) considered in this study. Circle diameter corresponds to earthquake magnitude, and color refers to centroid depth. The number listed above each focal mechanism corresponds to the superscript in the event location column of Table 1.

3. Methods

We now explore the evolution of peak displacement amplitude as a proxy for moment evolution. Equation (1) expresses the relation between amplitude of displacement at the surface, *PGD*, hypocentral distance, *R*, and earthquake magnitude, M_w (e.g., Fowler, 2005). *A*, *B*, and *C* are constants to be estimated (Crowell et al., 2013; Wu & Zhao, 2006) given the known values of *PGD*, *R*, and M_w.

$$\log_{10}(PGD) = A + BM_w + C\log_{10}(R) \tag{1}$$

The distance attenuation term in equation (1), $C\log_{10}(R)$, is sufficient for a point-source approximation of rupture. While this assumption may hold for early observation times, later in rupture the interpretation of the rupture as a finite fault is required. To do so, we follow earlier studies, supplementing the distance term with a magnitude dependence (Crowell et al., 2013; Melgar et al., 2015):

Table 1
Event Information for the 14 Earthquakes Included in the Analysis

Location	M_w	Origin time (UTC)	Hypocenter			# GNSS
			Longitude (°E)	Latitude (°N)	Depth (km)	Stations
Tokachi-oki[1]	8.3	2003-9-25 19:50:07.64	144.0785	41.7797	42.0	217
Miyagi[2]	7.3	2011-3-9 02:45:12.97	143.2798	38.3285	8.3	286
Tohoku-oki[3]	9.1	2011-3-11 05:46:18.12	142.3730	38.2970	29.0	493
Iwate[4]	7.4	2011-3-11 06:08:53.05	142.7815	39.8390	31.7	201
Ibaraki[5]	7.9	2011-3-11 06:15:34.46	141.2653	36.1083	43.2	340
N. Honshu[6]	7.6	2011-3-11 06:25:44.04	144.8940	37.8367	34.0	567
Miyagi[7]	7.1	2011-4-7 14:32:43.43	141.9237	38.2028	60.7	700
E. Fukushima[8]	6.7	2011-4-11 08:16:12.02	140.6727	36.9457	6.4	450
N. Honshu[9]	7.2	2012-12-7 08:18:20.28	144.3153	37.8158	46.0	575
N. Honshu[10]	7.1	2013-10-25 17:10:18.39	144.5687	37.1963	56.0	273
Kumamoto[11]	6.2	2016-4-14 12:26:34.43	130.8087	32.7414	11.4	226
Kumamoto[12]	6.0	2016-4-14 15:03:46.45	130.7777	32.7007	6.7	201
Kumamoto[13]	7.0	2016-4-15 16:25:05.47	130.7630	32.7545	12.5	254
Kumamoto[14]	5.7	2016-4-15 16:45:55.45	130.8990	32.8632	10.6	177

Note. Superscript on location column corresponds to event number in Figure 1. Earthquake origin time and hypocenter location are from National Research Institute for Earth Science and Disaster Resilience. Origin time is given as year-month-day hour:minute:second. magnitude is from Global CMT (globalCMT.org). The right-hand column denotes the number of GNSS (Global Navigation Satellite System) stations recording the event within the area also covered by properly triggered strong-motion stations (for *P* wave arrival interpolation).

$$\log_{10}(PGD) = A + BM_w + CM_w \log_{10}(R) \tag{2}$$

Throughout the main text, we present results using the finite fault interpretation of equation (2). For completeness, we include an additional set of results for the point-source assumption (equation (1)) in the supporting information.

We have modified the scaling equations to include a weight matrix, W, that accounts for the different number of observations (data points) in different magnitude ranges. We divide the data into magnitude bins ($M_w < 7$, $7 < M_w < 7.5$, $7.5 < M_w < 8$, $8 < M_w < 8.5$, and $M_w > 8.5$) and weight by the inverse of the norm of PGDs in each bin. In this way, each bin becomes equally important in the resulting inversion and there is no bias toward preferentially fitting some part of the magnitude range spanned by more events or by larger signals. We include only measurements of PGD that are above the expected GNSS noise. A typical value is ~1 cm in the horizontal direction and ~5 cm in the vertical (Genrich & Bock, 2006). To avoid fitting stations whose observations do not exceed the noise, we remove all observations where PGD is smaller than 4 cm. Once a station's maximum observed displacement has exceeded 4 cm, it is introduced into the regression.

Coefficients A, B, and C in equations (1) and (2) can be estimated from the observations at any point in time following P wave onset. We use an L1-norm minimization scheme (Melgar et al., 2015), to reduce sensitivity to outliers. We first construct the total displacement waveform as a function of time, $D(t)$, at each station such that

$$D(t) = \left(N(t)^2 + E(t)^2 + \mathrm{U}(t)^2\right)^{½}, \tag{3}$$

where $N(t)$, $E(t)$, and $U(t)$ are the north-south, east-west, and up-down displacement waveforms, respectively. PGD as a function of time is then the maximum of $D(t)$, observed up to a given epoch.

$$PGD(t) = \max\left[D(\tau)\right]; 0 < \tau \leq t, \tag{4}$$

where 0 denotes the P wave arrival time at a particular station. P wave onsets at each GNSS station are interpolated from the arrival times observed at nearby strong-motion sites (Figure 2). For the time-dependent regression (equations (1) and (2)) we study the scaling properties of PGD observed over increasing windows following P wave onset. We begin with a window of only 5 s (to investigate earthquake onset observations) and expand the window in 5-s intervals up to a final value of 170 s, when the final value of PGD(t) is achieved

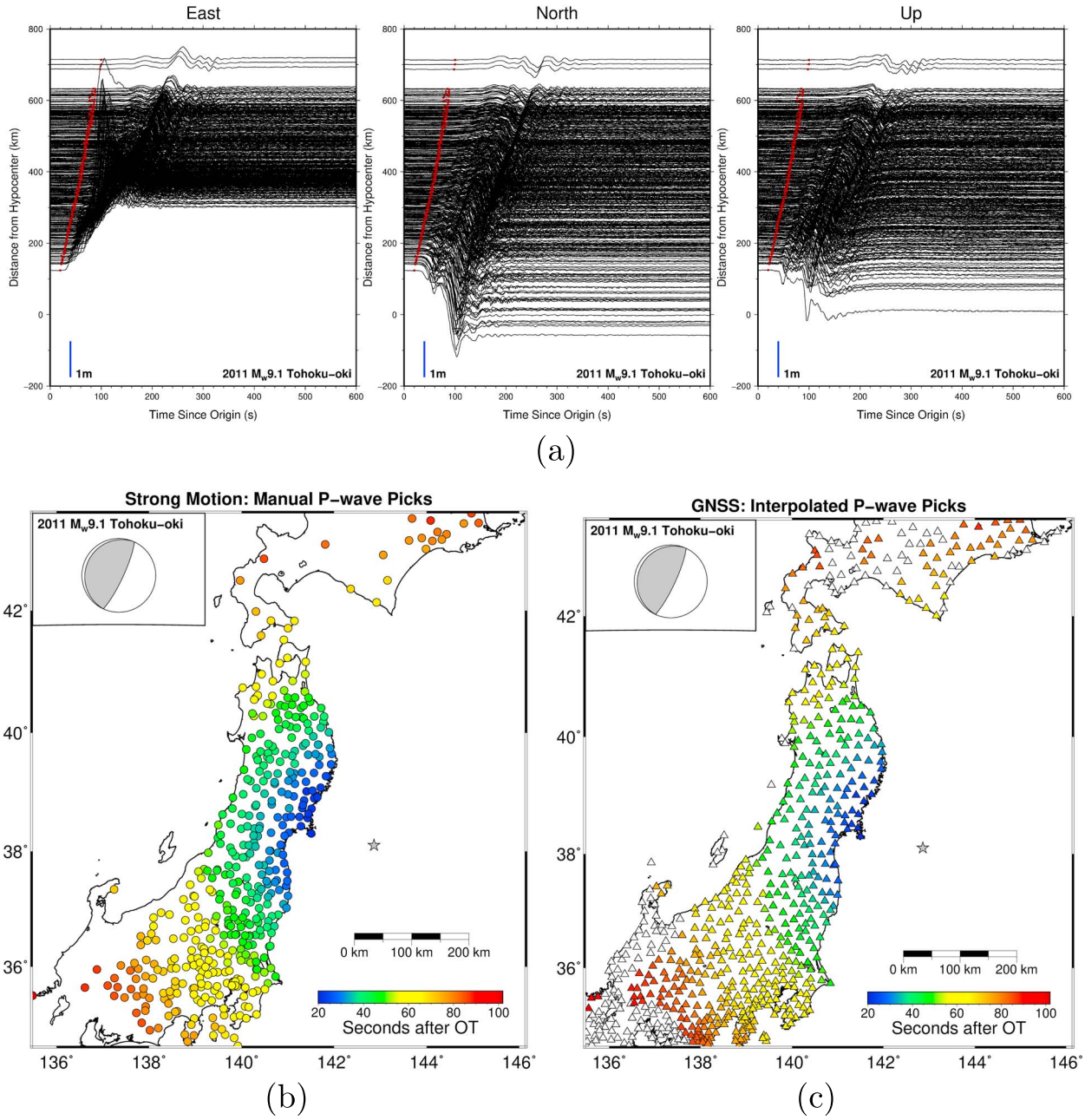

Figure 2. Example earthquake data set, 2011 M_w9.1 Tohoku-oki earthquake. (a) Precise point positioning solutions for the three components of motion (left: east, center: north, right: up) for all GNSS stations included in our analysis. Waveforms are offset by hypocentral distance. Red dots denote the *P* wave arrival time assigned from (c). (b) Strong-motion seismic station locations (circles), colored by manually picked *P* wave arrival times. (c) Available GNSS stations (triangles). Colored stations are within the footprint covered by strong-motion *P* wave picks and have been assigned a *P* wave arrival time via interpolation from (b). White triangles are beyond the region covered by strong-motion *P* wave picks and are not included in subsequent analysis. Earthquake epicenter is denoted by gray star, with associated focal mechanism in the top left corners of (b) and (c). The corresponding information for the other considered earthquakes is given in Figures S1–S13. GNSS = Global Navigation Satellite System.

for all events and distances considered. For each 5-s window we carry out a regression for the best fitting set of coefficients (*A*, *B*, and *C*, equations (1) and (2)). These coefficients at each 5-s interval are calculated by randomly removing 10% of the stations from each earthquake, solving the regression, and repeating 100 times. In each iteration, we test the reliability of the relationship by invoking the removed 10% of stations to estimate each earthquake's magnitude for the relationship derived from the other 90% of data. We assess the amount of data subsequent to the *P* wave arrival required for reliable magnitude estimation.

This is different from previous approaches (Crowell et al., 2013, 2016; Melgar et al., 2015), which have generated one set of coefficients with the final value of PGD. In our formulation, *A*, *B*, and *C* vary as a function of time, hence PGD(*t*).

4. Results and Discussion

4.1. Evolution of Maximum Displacement

We performed the PGD(*t*) analysis for the 14 earthquakes in Japan (Table 1). Figure 3 illustrates the best fitting relationships at several times after *P* wave onset, beginning with only 5 s of data (Figure 3a) and increasing by 15 s in subsequent panels. Details of the best fitting coefficients at each time step (equation (2)) are available in Table S1. For the same analysis using a point-source assumption (equation (1)), see supporting information Figure S14 and Table S2. At 5 s, only a small number of PGD observations exceed the noise threshold of 4 cm (Figure 3a); thus, the best fitting PGD(*t*) relationships cannot be considered reliable and we are limited in drawing conclusions about these early stages. In each iteration, 10% of the data were removed prior to inversion for the scaling coefficients (*A*, *B*, and *C*). The estimated coefficients were then applied to the removed 10% to test reliability. The standard deviation of the residuals between known magnitude and calculated magnitude of the removed 10% is listed in the right-hand column of Table S1. We require 20 s of data after the *P* waves have arrived before the best fitting relation allows estimation within 1 magnitude unit (one sigma) and 55 s of data before the residual consistently comes within 0.5 magnitude units. The final error is ±0.36 magnitude units, consistent with previous studies (Melgar et al., 2015). The size of the error implies that earthquake magnitude is indistinguishable from observations of displacement amplitude early in rupture but becomes more reliable as stations record their final PGD value. As the evolution of peak displacement progresses, it is visually clear that magnitude is differentiated when displacement amplitude recorded from the smaller of the two earthquakes has achieved PGD, and the PGD(*t*) observations from the larger earthquake continue to increase. This is perhaps clearest in Figure 3c; all earthquakes $< M_w8$ appear separated, but the two largest events (2003 $M_w8.3$ Tokachi-oki and 2011 $M_w9.1$ Tohoku-oki) have overlapping distributions of data points. By Figure 3e, the GNSS stations nearest the $M_w8.3$ event (orange) have recorded peak displacement and are now exceeded by the observations of the $M_w9.1$ (red) at the same hypocentral distances. As the later, highest amplitude seismic waves continue to propagate, this separation becomes apparent at increasing distances in subsequent panels. Similarly, because we do not see evidence of separation prior to final PGD, the best fitting scaling relations are poor at earlier stages. Evidence of the insufficient fit is notable in Figures 3e–3g, where the $M_w9.1$ observations (red) approach the best fit line for $M_w = 10$.

The timing of separation between events of different magnitudes is consistent with the amount of time it takes for the smaller of any two compared events to reach PGD. Our findings are therefore in agreement with the notion of universal initial (over the first few seconds) rupture behavior regardless of final magnitude. That is, these geodetic observations do not support the idea of strong determinism from earthquake onset parameters. However, we acknowledge limitations in the availability of near-fault data from the larger events in our study. Next, we consider the case for weak determinism at later rupture times.

4.2. Observational Timing of PGD

We find that final PGD is the first reliable proxy for magnitude; therefore, we must then address when, with respect to rupture initiation, we expect to observe final PGD. The answer places a lower limit on the timeliness of accurate magnitude estimation and contributes to our understanding of earthquake development and determinism. Figure 4 shows the relationship between timing of PGD and hypocentral distance for a subset of the earthquakes considered (those with wide hypocentral distance coverage). The black dashed line denotes an estimate of the duration between *P* and *S* wave (*S*-*P*) arrival times at each distance for a 1-D velocity model (Table S3). *S* waves are responsible for larger ground motion; thus, this line denotes the lower bound of the timing of PGD with respect to the *P* wave arrival. Assuming the same Earth structure for each event, maximum ground displacement should follow shortly after this demarcation, regardless of earthquake size. From the observational data in Figure 4, two major features are apparent: First, the largest event ($M_w9.1$, red) takes considerably longer than the smaller events to reach PGD even at the same hypocentral distances, a feature previously noted in studies using strong-motion observations (e.g., Colombelli et al., 2012), and second, for the remaining events, the observed time to PGD follows a trend with a shallower slope than the *S*-*P* line at short distances but becomes similarly steep to that line at greater distances. Finally, the hypocentral

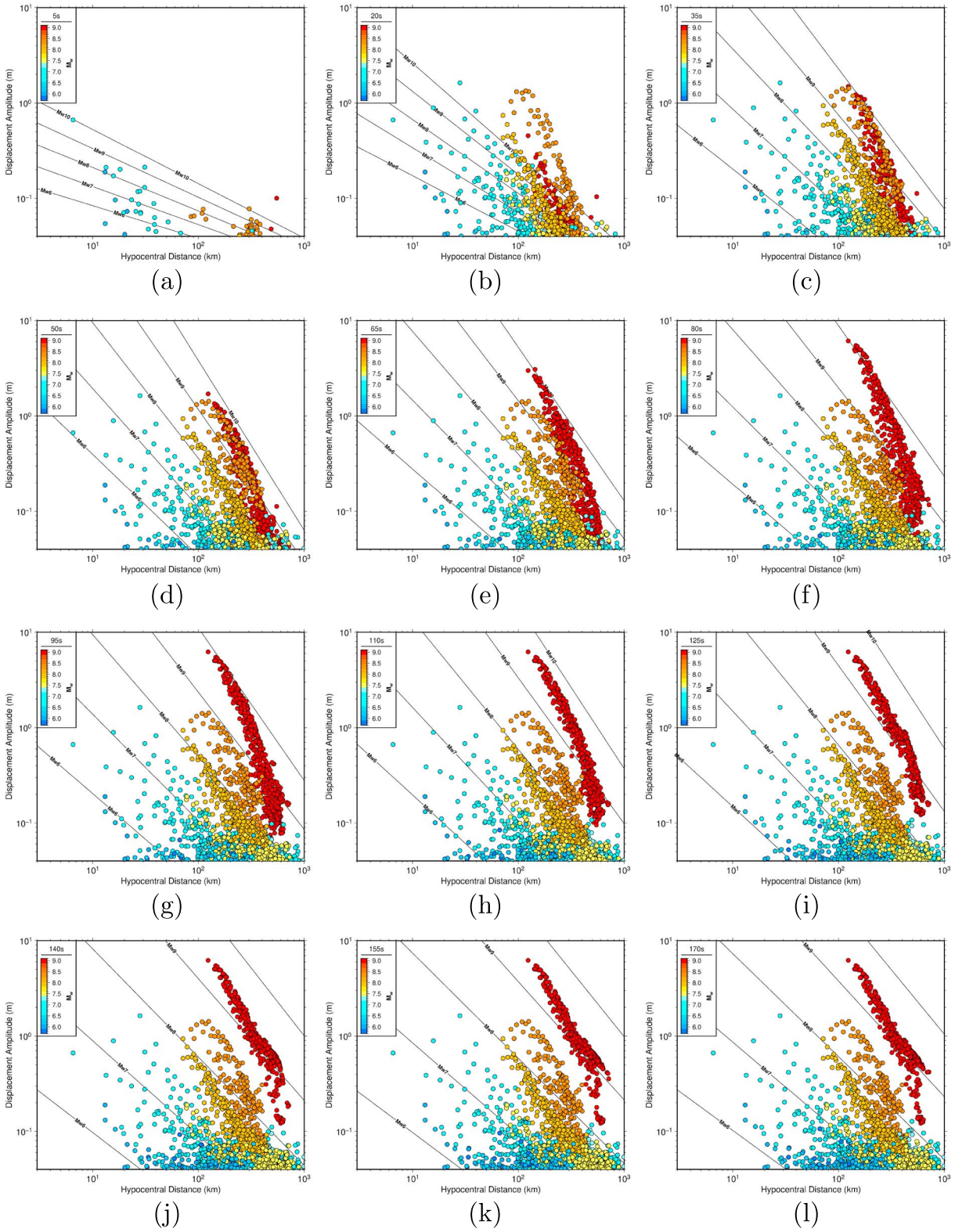

Figure 3. Best fitting magnitude scaling relations for the 14 considered events assuming a finite fault (equation (2)). Each panel illustrates the relation between hypocentral distance and the maximum displacement amplitude observed within the following time windows after *P* wave arrival: (a) 5 s, (b) 20 s, (c) 35 s, (d) 50 s, (e) 65 s, (f) 80 s, (g) 95 s, (h) 110 s, (i) 125 s, (j) 140 s, (k) 155 s, and (l) 170 s. Each colored circle represents a single station and is colored based on the magnitude of the observed earthquake. Black lines denote the relation described by the best fitting coefficients *A, B,* and *C* at each time interval shown. The lower limit of the *y* axis is 4 cm, the chosen Global Navigation Satellite System noise floor.

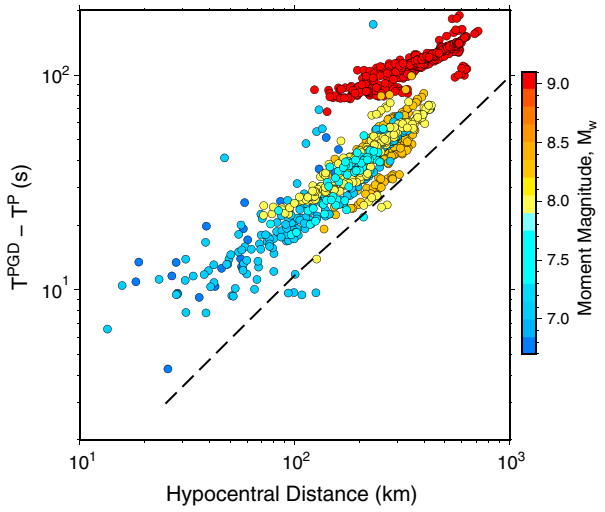

Figure 4. Relationship between hypocentral distance and the time from *P* wave arrival to final peak ground displacement (PGD) for a subset of the earthquakes considered; those with wide hypocentral distance coverage. Black dashed line is the expected *S* wave arrival minus *P* wave arrival (*S-P*) time for a 1-D velocity model (Table S2) and 25-km source depth. Each colored circle represents a single station and is colored based on the magnitude of the observed earthquake.

distance at which the slope changes from shallower than the *S-P* line to similar to the *S-P* line is greater for larger-magnitude events. The data points that appear below the *S-P* line may be due to a more complex velocity structure or low PGD amplitudes exceeded by GNSS noise earlier in the time series.

Considering that the largest earthquakes are offshore thrust events, they are primarily observed at long distances, with most observations further than 100 km from the hypocenter. However, understanding this relationship at smaller hypocentral distances is a crucial step toward discerning the minimum amount of time required to accurately measure PGD, and subsequently, estimate earthquake magnitude. We consider the physical basis for the observed relationship between hypocentral distance and time to PGD. We hypothesize that at close distances, a station is most sensitive to slip on the portion of the finite fault closest to it, rather than the rupture surface as a whole. Displacement then should be related to the local duration of slip, or rise time. In turn, sites farther afield will be sensitive to the integrated signal from the fault as a whole, and thus, time to PGD will be related to the source duration. In other words, for distant stations, the fault can be approximated as a point source, while at closer stations, heterogeneity of the finite fault becomes important. This transition point from near to far field will depend on the frequency content of the radiated signal. The distance from the fault at which this change occurs may account for the observed change in slope in Figure 4.

Galetzka et al. (2015) demonstrated that near-field high-rate GNSS recordings of the 2015 M_w7.8 Nepal earthquake were most consistent with kinematic rupture characterized by a simple slip pulse. Similarly, Melgar and Hayes (2017) reported that rise time scales with earthquake magnitude. From these observations we further hypothesize that the observed pattern in Figure 4 is in part due to the different average rise times associated with increasing magnitude of these events. The notion of magnitude-dependent rise time is consistent with a weakly deterministic rupture model in which rupture organizes within the first tens of seconds into a slip pulse that has a width diagnostic of magnitude.

4.3. Synthetic Modeling of PGD Time

To examine the influence of rise time on the timing of peak displacement, we supplement the observations with synthetic modeling using the SW4 software (geodynamics.org/cig/software/sw4, Petersson & Sjögreen, 2017a, 2017b). This allows us to specifically test the rupture characteristics that we hypothesize are responsible for our observations of PGD(*t*) and gain insight into behavior at distances not covered by our observational data set. We test a simple model of a north-south striking, 20° west dipping thrust fault with homogeneous slip. Rupture begins at the center of the fault and propagates bilaterally toward the northern and southern ends. A grid of receivers is located along the overriding plate. Figure 5 depicts a schematic of the model setup. Our testing includes five models with varying magnitude (M_w6.5, M_w7.0, M_w7.5, M_w8.0, and M_w8.5). Each model differs from the others in two magnitude-dependent ways: Fault dimensions (length and width) are determined from the subduction zone rupture scaling laws of Blaser et al. (2010), and the average rise time for each event is assigned from the scaling relation described in Melgar and Hayes (2017). Rupture speed is held fixed at 2.8 km/s, and thus, we assume that each of these models is a bilateral propagating slip pulse. We assume a 1-D Earth structure, given in Table S3. Receivers measure displacement and are located in an evenly spaced grid, between 25 and 500 km from the hypocenter.

Figure 6 shows the expected timing of PGD relative to the *P* wave arrival for our suite of tests. At close distances, it is apparent that longer rise times and larger fault dimensions are associated with delayed PGDs. Indeed, this is the case on a station-by-station basis for all stations within ~150 km of the hypocenter. Beyond that distance, surface waves become dominant, obscuring the pattern. Second, there appear to be two disparate slopes, one in the near-field and one in the far field, similar to what is observed in the PGD measurements from GNSS displacement data (Figure 4). The location of the change between slopes appears to be

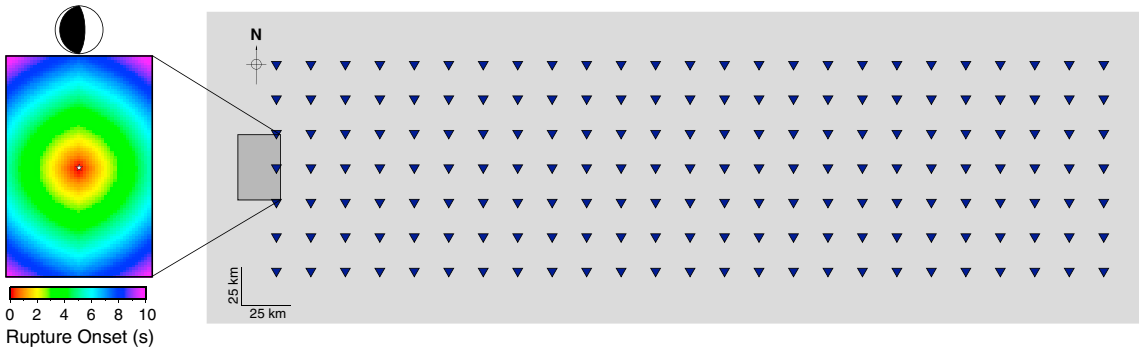

Figure 5. Schematic of model design, shown here for the M_w7.0 test. The bilateral propagating fault strikes north-south and dips 20° west (see focal mechanism, top left). Dip-slip (thrust) motion is uniform across the fault, with rupture onset determined by a rupture propagation velocity of 2.8 km/s. Fault is colored by rupture onset time, with white star representing the hypocenter location, at 25-km depth. Inverted triangles denote the receiver locations where synthetic observations are made. For larger-magnitude input models, rows of receivers are added to the north and south of those shown, spanning at least 0.5 fault lengths to the north and south of the fault limits.

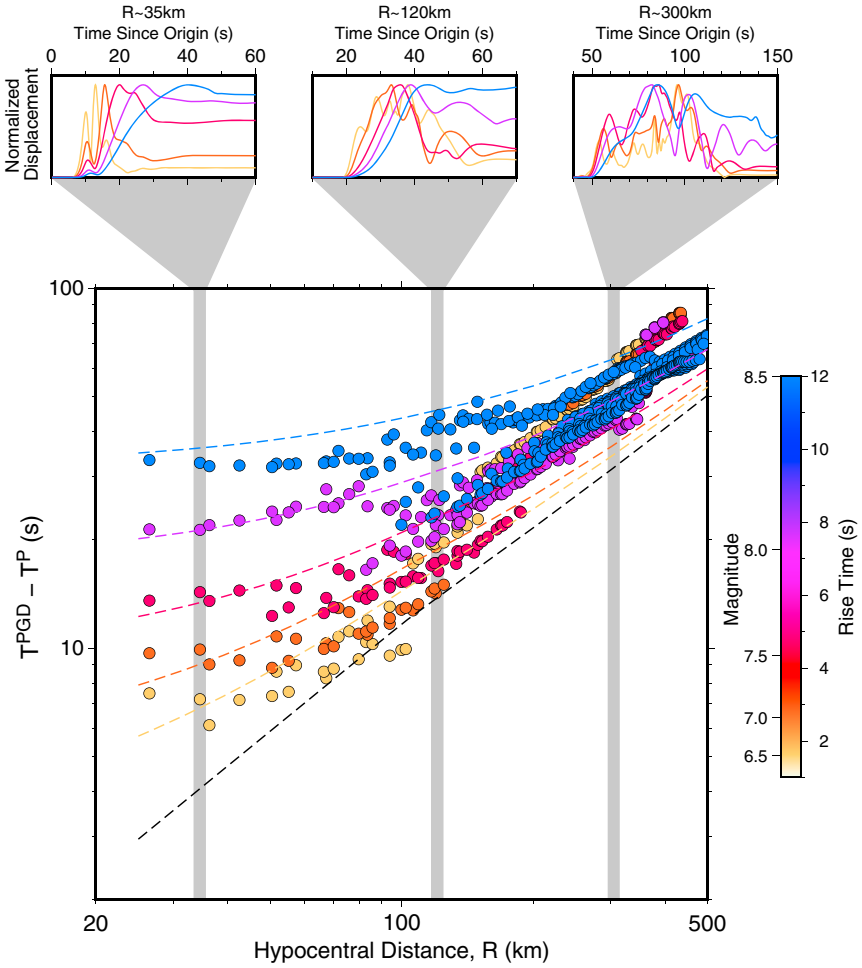

Figure 6. Timing of peak ground displacement relative to *P* wave arrival time as a function of distance from the hypocenter for a bilateral rupture propagation. Earthquakes are modeled from M_w6.5 to M_w8.5, in 0.5 magnitude unit intervals, with associated fault dimensions (Blaser et al., 2010) and rise times (Melgar & Hayes, 2017). Each circle represents observations from a single receiver and is colored by the rise time of the modeled earthquake. The black dashed line is the *S-P* travel time for the 1-D velocity model (Table S3) and 25-km source depth. Colored dashed lines represent the value of the half duration of rupture added to the *S-P* travel time. Above, examples of waveforms from receivers at three representative hypocentral distances show the pattern of timing of peak ground displacement for the different rise time events. Each waveform is normalized to its corresponding peak ground displacement.

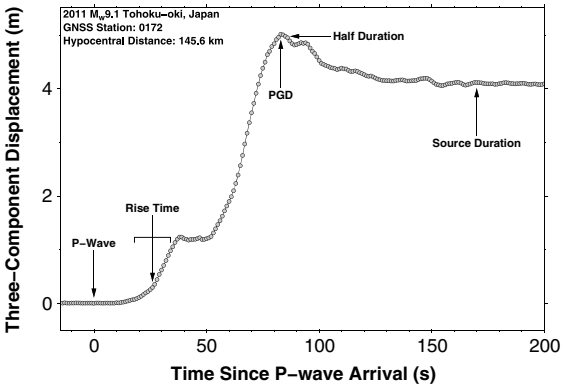

Figure 7. Time series of GNSS-derived displacements for GEONET station 0172, detailing the timing of earthquake parameters relative to the *P* wave arrival during the 2011 M_w9.1 Tohoku-oki earthquake. Earthquake source duration is from the U.S. Geological Survey finite-fault source time function (Hayes, 2017) with average rise time (arrow) and standard deviation (bracket) from Melgar and Hayes (2017). GNSS = Global Navigation Satellite System; GEONET = GNSS Earth Observation Network.

related to magnitude as well, with this transition point occurring at greater hypocentral distances for larger magnitudes. Equation (1), which assumes a point source, is better equipped at distances beyond this change in slope, where the finite fault dimensions are small compared to the distance between source and receiver. Modifications are likely required to properly assess observations in the near field.

Figure 6 provides insight into how early it might be possible to determine magnitude from PGD measurements. The black dashed line indicates the *S-P* travel time for the assumed velocity model and a source depth of 25 km. The colored dashed lines in Figure 6 correspond to the sum of the *S-P* value and half duration for the event of the same color. The M_w6.5 event has a rupture duration of only 5.5 s and is complete prior to any PGD observations at the receiver stations. The M_w7.0 has a duration comparable to the time required to observe PGD, about 10 s. Above M_w7.0, there is a consistent pattern demonstrating that at close enough distances, the PGD metric is available prior to rupture completion. In the case of the M_w8.5 event, though rupture lasts ~65 s, only about 35 s of observations following the *P* wave are required to observe PGD at stations within ~90 km of the hypocenter. Thus, our findings are consistent again with a weakly deterministic earthquake rupture model, wherein metrics that can differentiate the earthquake magnitude are available tens of seconds after first observations and before completion of rupture. Our model is simplistic in its assumption of homogeneous slip, whereas a fault is more likely to experience heterogeneity in both slip and rise time, leading to additional variation in the timing of PGD observation. Thus, our model represents an average of the expected behavior for earthquakes of the represented magnitudes.

We further demonstrate the timing of relevant parameters with an example displacement time series observed at GNSS station 0172, located 145.6 km from the 2011 M_w9.1 Tohoku-oki earthquake (Figure 7). We denote the timing of the final observed PGD relative to the *P* wave arrival, as well as the length of earthquake source properties including rise time, half duration, and source duration relative to the *P* wave arrival. For the Tohoku-oki event, the full source duration is 170 s (Hayes, 2017) and the average rise time is 26 s with a standard deviation of 8 s (Melgar & Hayes, 2017). For this M_w9.1 event, the PGD metric is observed in slightly less time than the earthquake half duration, even at a hypocentral distance of almost 150 km.

Large events most likely behave like slip pulses (Heaton, 1990; Melgar & Hayes, 2017) with rise time and width that scale with the eventual final magnitude of the event. Furthermore, GNSS stations will be most sensitive to the portion of the fault closest to them. As a result, we suggest that at close distances, stations are not required to observe the complete rupture in order to have magnitude-identifying qualities. Rather, they must only observe the passing of the slip pulse, which is much shorter in duration than the full earthquake rupture. Thus, if stations are available close enough to the source, it will be possible to infer the magnitude of an earthquake prior to rupture completion. While our simulation was conducted for a thrust faulting environment, there is evidence that this pulse-slip behavior is exaggerated for long, narrow faults, such as continental strike-slip faults (Day, 1982; Zheng & Rice, 1998). Thus, our findings are especially relevant to the ongoing implementation of earthquake early warning in California, USA (Kohler et al., 2017). Evidence of weak determinism places enormous importance on the location of receivers capable of both timing the *P* wave arrival (typically seismic instrumentation) and measuring accurate PGD (typically geodetic instrumentation) in near-fault locations and in real time. In the continental strike-slip regions, real-time networks have been designed to instrument the near-fault regions. For large subduction zone earthquakes that rupture mostly offshore and pose tsunami risk, such near-field measurements remain a challenge. It reinforces the need for real-time offshore seismic and geodetic instrumentation such as ocean bottom strong-motion seismometers, absolute pressure gauges, and GPS-acoustic positioning to improve earthquake and tsunami early warning (e.g., Imano et al., 2015; Saito & Tsushima, 2016; Takahashi et al., 2015; Yokota et al., 2016; Yoshioka & Matsuoka, 2013).

5. Conclusions

Reliable magnitude estimation from early earthquake onset properties (~5 s) is not supported by our geodetic observations. However, earthquake magnitude is discernible prior to rupture completion of the largest events using GNSS-derived peak displacements, indicating a weak determinism. Furthermore, the relationship between source-receiver distance and timing of maximum displacement amplitude demonstrate that our geodetic observations are consistent with a previously proposed source model describing rupture as a slip pulse of magnitude-dependent width. Changes in slip pulse width affect the timing of PGD observations. This timing provides a measure of the observation length required to compute an accurate magnitude estimate. Our findings suggest that high priority should be placed on installation of near-fault seismogeodetic instrumentation capable of both *P* wave arrival detection and accurate displacement measurements, including ocean bottom seismometers, pressure sensors, and GPS-acoustic seafloor instruments.

Acknowledgments
We thank Aldo Zollo, Thomas Hanks, and one anonymous reviewer for their thoughtful comments. We gratefully acknowledge funding support from the National Aeronautics and Space Administration grants NNX14AQ53G, NNX16AM04A, and NNX13AT33G to UC San Diego, from the Gordon and Betty Moore Foundation grant GBMF3024 to UC Berkeley, and from the U.S. Geological Survey grants G16AC00348 and G17AC00346 to UC Berkeley. We thank the Geospatial Information Authority of Japan for the GNSS data and maintenance of the GNSS Earth Observation Network as well as the National Research Institute for Earth Science and Disaster Resilience for maintenance of the strong-motion networks, KiK-net and K-net. The GPS time series for the earthquakes studied are available at ftp://garner.ucsd.edu/pub/projects/Select_GNSS_Displacements-Japan/.

References

Blaser, L., Krüger, F., Ohrnberger, M., & Scherbaum, F. (2010). Scaling relations of earthquake source parameter estimates with special focus on subduction environment. *Bulletin of the Seismological Society of America*, *100*(6), 2914–2926. https://doi.org/10.1785/0120100111

Bock, Y., Melgar, D., & Crowell, B. W. (2011). Real-time strong-motion broadband displacements from collocated GPS and accelerometers. *Bulletin of the Seismological Society of America*, *101*(6), 2904–2925. https://doi.org/10.1785/0120110007

Boore, D. M., Stephens, C. D., & Joyner, W. B. (2002). Comments on baseline correction of digital strong-motion data: Examples from the 1999 Hector Mine, California, earthquake. *Bulletin of the Seismological Society of America*, *92*(4), 1543–1560. https://doi.org/10.1785/0120000926

Colombelli, S., Zollo, A., Festa, G., & Kanamori, H. (2012). Early magnitude and potential damage zone estimates for the great M_w9 Tohoku-Oki earthquake. *Geophysical Research Letters*, *39*, L22306. https://doi.org/10.1029/2012GL053923

Colombelli, S., Zollo, A., Festa, G., & Picozzi, M. (2014). Evidence for a difference in rupture initiation between small and large earthquakes. *Nature Communications*, *5*, 3958. https://doi.org/10.1038/ncomms4958

Crowell, B. W., Melgar, D., Bock, Y., Haase, J. S., & Geng, J. (2013). Earthquake magnitude scaling using seismogeodetic data. *Geophysical Research Letters*, *40*, 6089–6094. https://doi.org/10.1002/2013GL058391

Crowell, B. W., Schmidt, D. A., Bodin, P., Vidale, J. E., Gomberg, J., Renate Hartog, J., et al. (2016). Demonstration of the Cascadia G-FAST geodetic earthquake early warning system for the Nisqually, Washington, earthquake. *Seismological Research Letters*, *87*, 930–-943. https://doi.org/10.1785/0220150255

Day, S. M. (1982). Three-dimensional simulation of spontaneous rupture: the effect of nonuniform prestress. *Bulletin of the Seismological Society of America*, *72*(6A), 1881–1902.

Fowler, C. M. R. (2005). *The solid earth: An introduction to global geophysics* (2nd ed.). Cambridge: Cambridge University Press.

Galetzka, J., Melgar, D., Genrich, J. F., Geng, J., Owen, S., Lindsey, E. O., et al. (2015). Slip pulse and resonance of the Kathmandu basin during the 2015 Gorkha earthquake, Nepal. *Science*, *349*(6252), 1091–1095. https://doi.org/10.1126/science.aac6383

Geng, J., Bock, Y., Melgar, D., Crowell, B. W., & Haase, J. S. (2013). A new seismogeodetic approach applied to GPS and accelerometer observations of the 2012 Brawley seismic swarm: Implications for earthquake early warning. *Geochemistry, Geophysics, Geosystems*, *14*, 2124–2142. https://doi.org/10.1002/ggge.20144

Genrich, J. F., & Bock, Y. (2006). Instantaneous geodetic positioning with 10–50 Hz GPS measurements: Noise characteristics and implications for monitoring networks. *Journal of Geophysical Research*, *111*, B03403. https://doi.org/10.1029/2005JB003617

Goldberg, D., & Bock, Y. (2017). Self-contained local broadband seismogeodetic early warning system: Detection and location. *Journal of Geophysical Research: Solid Earth*, *122*, 3197–3220. https://doi.org/10.1002/2016JB013766

Hayes, G. P. (2017). The finite, kinematic rupture properties of great-sized earthquakes since 1990. *Earth and Planetary Science Letters*, *468*, 94–100. https://doi.org/10.1016/j.epsl.2017.04.003

Heaton, T. H. (1990). Evidence for and implications of self-healing pulses of slip in earthquake rupture. *Physics of the Earth and Planetary Interiors*, *64*(1), 1–20. https://doi.org/10.1016/0031-9201(90)90002-F

Hoshiba, M., & Ozaki, T. (2014). Earthquake early warning and tsunami warning of the Japan meteorological agency, and their performance in the 2011 off the Pacific coast of Tohoku earthquake (*Mw* 9.0). In F. Wenzel & J. Zschau (Eds.), *Early warning for geological disasters* (pp. 1–28). Berlin: Springer. https://doi.org/10.1007/978-3-642-12233-0_1

Imano, M., Kido, M., Ohta, Y., Fukuda, T., Ochi, H., Takahashi, N., & Hino, R. (2015). Improvement in the accuracy of real-time GPS/acoustic measurements using a multi-purpose moored buoy system by removal of acoustic multipath. In M. Hashimoto (Ed.), *International Symposium on Geodesy for Earthquake and Natural Hazards (GENAH)* (Vol. 145, pp. 105–114). Switzerland: Springer. https://doi.org/10.1007/1345_2015_192

Kohler, M. D., Cochran, E. S., Given, D., Guiwits, S., Neuhauser, D., Henson, I., et al. (2017). Earthquake early warning ShakeAlert system: West coast wide production prototype. *Seismological Research Letters*, *89*(1), 99–107. https://doi.org/10.1785/0220170140

Meier, M. A., Ampuero, J., & Heaton, T. H. (2017). The hidden simplicity of subduction megathrust earthquakes. *Science*, *357*(6357), 1277–1281 . https://doi.org/10.1126/science.aan5643

Meier, M. A., Heaton, T., & Clinton, J. (2016). Evidence for universal earthquake rupture initiation behavior. *Geophysical Research Letters*, *43*, 7991–7996. https://doi.org/10.1002/2016GL070081

Melgar, D., Bock, Y., & Crowell, B. W. (2012). Real-time centroid moment tensor determination for large earthquakes from local and regional displacement records. *Geophysical Journal International*, *188*(2), 703–718. https://doi.org/10.1111/j.1365-246X.2011.05297.x

Melgar, D., Crowell, B. W., Geng, J., Allen, R. M., Bock, Y., Riquelme, S., et al. (2015). Earthquake magnitude calculation without saturation from the scaling of peak ground displacement. *Geophysical Research Letters*, *42*, 5197–5205. https://doi.org/10.1002/2015GL064278

Melgar, D., & Hayes, G. P. (2017). Systematic observations of the slip pulse properties of large earthquake ruptures. *Geophysical Research Letters*, *44*, 9691–9698. https://doi.org/10.1002/2017GL074916

Olson, E. L., & Allen, R. M. (2005). The deterministic nature of earthquake rupture. *Nature*, *438*(7065), 212–215. https://doi.org/10.1038/nature04214

Petersson, N. A., & Sjögreen, B. (2017a). *SW4 v2.0*. Davis, CA: Computational Infrastructure of Geodynamics. https://doi.org/10.5281/zenodo.1045297

Petersson, N. A., & Sjögreen, B. (2017b). *User's guide to SW4, version 2.0. Technical report LLNL-SM-741439*. Livermore, CA: Lawrence Livermore National Laboratory.

Rydelek, P., & Horiuchi, S. (2006). Earth science: Is earthquake rupture deterministic? *Nature*, *442*(7100), E5–E6. https://doi.org/10.1038/nature04963

Saito, T., & Tsushima, H. (2016). Synthesizing ocean bottom pressure records including seismic wave and tsunami contributions: Toward realistic tests of monitoring systems. *Journal of Geophysical Research: Solid Earth*, *121*, 8175–8195. https://doi.org/10.1002/2016JB013195

Saunders, J. K., Goldberg, D. E., Haase, J. S., Bock, Y., Offield, D. G., Squibb, M. B., Restrepo, J. I., et al. (2016). Seismogeodesy using GNSS and low-cost MEMS accelerometers: Perspectives for earthquake early warning and rapid response. *Bulletin of the Seismological Society of America*, *106*(6), 2469–2489. https://doi.org/10.1785/0120160062

Takahashi, N., Ishihara, Y., Fukuda, T., Ochi, H., Tahara, J. I., Mori, T., et al. (2015). Buoy platform development for observation of tsunami and crustal deformation. In M. Hashimoto (Ed.), *International Symposium on Geodesy for Earthquake and Natural Hazards (GENAH)* (Vol. 145, pp. 97–103). Cham: Springer. https://doi.org/10.1007/1345_2015_114

Trifunac, M., & Todorovska, M. (2001). A note on the useable dynamic range of accelerographs recording translation. *Soil Dynamics and Earthquake Engineering*, *21*(4), 275–286. https://doi.org/10.1016/S0267-7261(01)00014-8

Wu, Y. M., & Zhao, L. (2006). Magnitude estimation using the first three seconds *P*-wave amplitude in earthquake early warning. *Geophysical Research Letters*, *33*, L16312. https://doi.org/10.1029/2006GL026871

Yokota, Y., Ishikawa, T., Watanabe, S., Tashiro, T., & Asada, A. (2016). Seafloor geodetic constraints on interplate coupling of the Nankai Trough megathrust zone. *Nature*, *534*(7607), 374. https://doi.org/10.1038/nature17632

Yoshioka, S., & Matsuoka, Y. (2013). Interplate coupling along the Nankai Trough, southwest Japan, inferred from inversion analyses of GPS data: Effects of subducting plate geometry and spacing of hypothetical ocean-bottom GPS stations. *Tectonophysics*, *600*, 165–174. https://doi.org/10.1016/j.tecto.2013.01.023

Yun, N. Y., & Hamada, M. (2014). Evacuation behavior and fatality rate during the 2011 Tohoku-Oki Earthquake and Tsunami. *Earthquake Spectra*, *31*(3), 1237–1265.

Zheng, G., & Rice, J. R. (1998). Conditions under which velocity-weakening friction allows a self-healing versus a cracklike mode of rupture. *Bulletin of the Seismological Society of America*, *88*(6), 1466–1483.

Zollo, A., Lancieri, M., & Nielsen, S. (2006). Earthquake magnitude estimation from peak amplitudes of very early seismic signals on strong motion records. *Geophysical Research Letters*, *33*, L23312. https://doi.org/10.1029/2006GL027795

Zumberge, J., Heflin, M., Jefferson, D., Watkins, M., & Webb, F. H. (1997). Precise point positioning for the efficient and robust analysis of GPS data from large networks. *Journal of Geophysical Research*, *102*(B3), 5005–5017. https://doi.org/10.1029/96JB03860